


Article

Multi-Walled Carbon Nanotubes Modified NiCo₂S₄ for the Efficient Photocatalytic Reduction of Hexavalent Chromium

Qiu Jin, Ziyue Zheng, Yuxiao Feng, Shuang Tian and Zuoli He * 

Shandong Key Laboratory of Water Pollution Control and Resource Reuse, School of Environmental Science and Engineering, Shandong University, Qingdao 266237, China; jinqiu20172124058@163.com (Q.J.); 202232966@mail.sdu.edu.cn (Z.Z.); 202212863@mail.sdu.edu.cn (Y.F.); tianshuang610@163.com (S.T.)

* Correspondence: zlhe@sdu.edu.cn

Abstract: Hexavalent chromium (Cr(VI)) compounds are considered to be occupational carcinogens, which can be transferred from the environment to the human body and pose a significant threat to human health. It is particularly urgent to explore a more efficient catalyst for removing Cr(VI) to comply with discharge standards. The addition of CNTs enables the separation and transfer of photogenerated charges. Thus, we synthesized a range of NiCo₂S₄ hybrid materials with different multi-walled carbon nanotube (MWCNTs) contents using a two-step hydrothermal method. The composites had significant advantages compared to pure NiCo₂S₄, such as an enhanced visible light absorption, increased specific surface area, high electron–hole pair separation, and fast electron transport. Thus, MWCNT addition enabled efficient photocatalytic performances in terms of reducing hexavalent chromium (Cr(VI)). Among all the composite samples, the MWCNT/NiCo₂S₄ with 0.050 g of MWCNTs achieved the highest efficiency in reducing Cr(VI) under light irradiation, which showed a removal rate close to 100% within 40 min. Such CNT-based composite photocatalysts could be used to reduce the highly toxic Cr(VI) in environmental applications.

Keywords: photocatalysis; hexavalent chromium; NiCo₂S₄; CNT; reduction



Citation: Jin, Q.; Zheng, Z.; Feng, Y.; Tian, S.; He, Z. Multi-Walled Carbon Nanotubes Modified NiCo₂S₄ for the Efficient Photocatalytic Reduction of Hexavalent Chromium. *C* **2023**, *9*, 99. <https://doi.org/10.3390/c9040099>

Academic Editor: Manuel Fernando Ribeiro Pereira

Received: 15 July 2023

Revised: 15 October 2023

Accepted: 17 October 2023

Published: 20 October 2023



Copyright: © 2023 by the authors. Licensee MDPI, Basel, Switzerland. This article is an open access article distributed under the terms and conditions of the Creative Commons Attribution (CC BY) license (<https://creativecommons.org/licenses/by/4.0/>).

1. Introduction

In the past decades, water resource pollution has become more and more severe with industrialization development [1]. Heavy metal pollution due to the massive application of heavy metals in industry is gaining widespread attention [2,3]. Among them, hexavalent chromium (Cr(VI)) is often used as an essential raw material in electroplating, pigment processing, leather making, photographic, textile, and other applications. Chromium is usually present in two different oxidation states, hexavalent chromium (Cr(VI)) and trivalent chromium (Cr(III)) [4,5]. Cr(III) is less toxic in the environment and plays a vital role in metabolic processes as a trace metal essential to human nutrition [6,7]. In addition, it can be readily precipitated out of wastewater as Cr(OH)₃ in an alkaline or neutral solution and removed as solid waste. Unfortunately, Cr(VI) is 100 times more toxic than Cr(III), which the US has classified as a top-rated toxic pollutant. This was by the Environmental Protection Agency (EPA) due to its dangerous persistence and extremely low degradability in water and soil. Thus, the reduction of Cr(VI) to Cr(III) is considered to be a critical step in the treatment of wastewater containing Cr(VI) [8–10]. In addition, Cr(VI) can quickly enter food chains and destroy human enzyme systems through ingestion, inhalation, or skin contact, which poses a considerable threat to human health [11,12]. Studies have shown that releasing potentially carcinogenic, highly toxic, and non-degradable Cr(VI) into the environment can cause health problems such as pulmonary gland obstruction, epidermal irritation, hepatitis, and cancer [11,13,14]. Therefore, the conversion of Cr(VI) into Cr(III) is a desirable method for strictly controlling the concentration of Cr(VI) in industrial wastewater so that the wastewater can be safely discharged.

Various conventional methods have been adopted to remove Cr(VI) from water environments, including ion exchange, adsorption, chemical reduction, bioremediation, physical reverse osmosis, and membrane separation [15–20]. However, traditional methods often result in ancillary contaminants, a high energy intake, and a low efficacy, which are relatively expensive and environmentally unfriendly [21,22]. Actual industrial wastewater is often treated using the chemical reduction method, which reduces Cr(VI) to Cr(III) by adding reducing agents (such as NaHSO₃, Na₂SO₃, and iron powder, etc.) to the wastewater, and then adding lime or sodium hydroxide for precipitation and separation [23,24]. The reducing agent needs to be added in an acidic environment, and the amount of reducing agent added must be more significant than the theoretical amount, but a large amount would cause the wastewater chemical oxygen demand to rise [25]. The main advantages of this method are its relatively mature technology, simple operation, low investment, and good results in engineering applications. However, it has a large amount of sludge and will produce secondary pollution, which is not in line with the development concept of green environmental protection.

Photocatalysis is a promising technology for achieving the one-step removal of Cr(VI) using sunlight due to its efficient, simple, and environmentally friendly features [26–29]. It has been extensively studied in environmental and energy fields [30–33]. More and more semiconductor photocatalysts [34] are being investigated and applied for Cr(VI) reduction, hydrogen production, carbon dioxide reduction, and the degradation of organic pollutants such as TiO₂ [35–38], g-C₃N₄ [39–41], ZnIn₂S₄ [42,43], NiCo₂S₄ [43], CuS [44], and BiVO₄ [39,45]. Unmodified photocatalysts tend to have a short photogenerated carrier lifetime and low specific surface area, leading to inefficient photocatalysis, which limits their development and practical application [46]. As an ideal additive phase for composite materials, carbon nanotubes (CNTs) have excellent electrical and mechanical properties, and their suitable pore size distribution allows for a better dispersion of metal components [43,47–50]. Moreover, their unique and stable structure and morphology, especially their surface properties, can be modified in different ways according to the needs of people, making them an ideal new catalyst carrier material [51]. The research on CNTs as catalyst carrier materials has mainly focused on loading active components onto CNTs [52–54]. In the photocatalysis of a single semiconductor, the photogenerated electrons migrate to the conduction band (CB) and then tend to return to the valence band (VB) again, which significantly reduces the photocatalytic efficiency. The addition of CNTs enables the separation and transfer of photogenerated charges [25,55]. In this study, CNTs were hybridized with NiCo₂S₄. CNTs as a carrier not only inhibited the aggregation of NiCo₂S₄ and increased the specific surface area of the catalysts, but also effectively inhibited the recombination of photogenerated carriers through charge transfer. The research content of this paper is instructive for the preparation and application of CNTs in photocatalysts.

Herein, a series of MWCNT-NiCo₂S₄ (C-NCS) composites with different MWCNT contents were prepared using a relatively facile two-step hydrothermal process. The synthesized composites were utilized for the photocatalytic reduction of Cr(VI) under UV-Visible radiation to evaluate their photocatalytic activity. The materials were characterized in detail using XRD, SEM, TEM, XPS, and BET, etc. The selective removal performance of the composites for Cr(VI) was also explored. Compared to the pure NiCo₂S₄, the composites with added MWCNTs showed a better photocatalytic activity. Among them, 0.050MWCNT-NiCo₂S₄ had the best performance in the photocatalytic reduction of Cr(VI).

2. Materials and Methods

2.1. Synthesis of Composite Photocatalysts

Firstly, 0.4 g of PVP (K30) was added to 50 mL of ultrapure water and ultrasonically dispersed well. In total, 0.050 g of multi-walled carbon nanotubes (MWCNTs) was added to the above solution, followed by 30 min of treatment using an ultrasonic reactor (SONICS VCX1500, SONICS & MATERIALS INC, 53 CHURCH HILL RD. NEWTOWN, CT, USA). The dispersion was stirred until it was cooled, then 0.1783 g of nickel chloride hexahydrate,

0.3568 g of cobalt chloride hexahydrate, 0.45 g of urea, and 10 mL of ultrapure water were added and stirred for 30 min. It was added to the hydrothermal kettle and reacted at 130 °C for 12 h. The obtained sample (precursor of 0.050C-NCS) was washed with ultrapure water and 75% alcohol and finally dried in an oven at 70 °C. In the second hydrothermal reaction step, 0.2 g of as-obtained product, 0.6 g of sodium sulfide nonahydrate, and 60 mL of ultrapure water were added to the hydrothermal kettle, sonicated for 2 min, stirred for 30 min, and then reacted hydrothermally at a temperature of 180 °C for 12 h. Similarly, various amounts of MWCNTs (0 g, 0.005 g, 0.020 g, 0.035 g, 0.050 g, 0.075 g, and 0.100 g) were added in the first step of the hydrothermal process to synthesize the MWNCT-NiCo₂S₄ composite samples. The obtained composite samples were named NCS, 0.005C-NCS, 0.020C-NCS, 0.035C-NCS, 0.050C-NCS, 0.075C-NCS, and 0.100C-NCS, respectively.

2.2. Photocatalytic Performance Measurements

The photocatalytic activity of the samples was evaluated by reducing Cr(VI) (K₂Cr₂O₇ solution). In this reaction, 15 mg catalysts were dispersed into 30 mL of 50 ppm Cr(VI) solution and then stirred in the dark for 30 min to reach the absorption–desorption equilibrium. Next, the suspension was irradiated with a 300 W Xenon lamp (CEL-HXF300-T3, Beijing China Education Au-Light Co., Ltd, Beijing, China) with a VisREF filter (350~780 nm). A total of 1 mL of sample was, intermittently and in specific time intervals, filtered through a 0.22 µm pore-sized PTFE syringe filter to determine the removal rate of Cr(VI). The concentration of Cr(VI) was determined with a UV-Vis spectrophotometer (Shimadzu UV2600, Shimadzu corporation, Nishinokyo Kuwabara-cho, Nakagyo-ku, Kyoto, Japan) using a diphenylcarbonyldihydrazide colorimetric method.

3. Results

3.1. Photocatalytic Performances

We synthesized NiCo₂S₄ nanoparticles with different MWCNT contents using a two-step hydrothermal method, adding 0 g, 0.005 g, 0.020 g, 0.035 g, 0.050 g, 0.075 g, and 0.100 g. The products obtained were defined as NCS, 0.005C-NCS, 0.020C-NCS, 0.035C-NCS, 0.050C-NCS, 0.075C-NCS, and 0.100C-NCS, respectively. The photocatalytic performances of the samples were evaluated using a 60 min reduction experiment of Cr(VI) with a controlled amount of photocatalyst under visible light irradiation, as shown in Figure 1a. A concentration of 30 mL of 50 ppm Cr(VI) was chosen for the photoreduction experiments. A schematic diagram of this reactor is demonstrated in Figure S1. The results showed that, when using pure NiCo₂S₄ as the photocatalyst, Cr(VI) could only be reduced by 64.4% in 60 min. However, all composites containing MWCNTs exhibited an excellent photocatalytic activity. In particular, 0.050C-NCS could reduce Cr(VI) entirely within 40 min, which exhibited the best photocatalytic performance. Figure 1b shows the results of the control experiment for the reduction of Cr(VI) by 0.050C-NCS, and it can be seen that the concentration of Cr(VI) was almost constant under light conditions only. At the same time, only 17.5% of Cr(VI) was adsorbed under dark conditions, and the MWCNT had almost no photocatalytic effect on Cr(VI), which further demonstrates the essential role of this composite in the photocatalytic reduction process of Cr(VI). Furthermore, the electron spin resonance (ESR) detection results (Figure S2) also indicated that a distinct ·O₂⁻ the characteristic signal peak was detected at 0.050C-NCS. In contrast, the detection of pristine NiCo₂S₄ indicated that the intensity of the O₂⁻ signal was significantly lower than that of 0.050C-NCS. This result also demonstrated an improvement in the photocatalytic performance when a certain amount of MWCNT was added. By verifying the effect of scavengers on photocatalytic efficiency, the active species with contributing roles in the photocatalytic process can be elucidated [56]. As shown in Figure S3, potassium bromate (10 mM) hindered the photocatalytic reduction process, which demonstrates that the photoelectrons were mainly responsible for the Cr(VI) photocatalytic reduction enhancement of the 0.050C-NCS. Furthermore, we compared the reaction conditions and reduction activity of different photocatalysts reported in the recent literature with the present work, and

the results are listed in Table S1. Compared to previous studies, 0.050C-NCS exhibited an excellent photocatalytic reduction of Cr(VI).

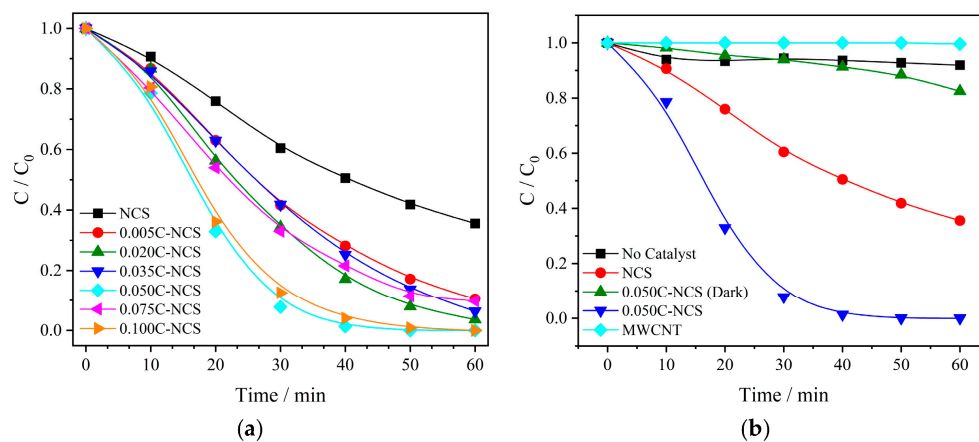


Figure 1. (a) Photocatalytic reduction curves of Cr(VI) in the presence of as-prepared samples with different amounts of MWCNTs (15 mg photocatalyst, 30 mL 50 ppm Cr(VI)); and (b) control experiment of photocatalytic reduction of Cr(VI) for 0.050C-NCS.

The separation rate of photogenerated electron–hole pairs is an essential factor affecting the photocatalytic activity of a photocatalyst. A higher separation efficiency of the photogenerated electron–hole pairs will result in a higher photocatalytic activity of the photocatalyst. To evaluate photocatalysts' charge carrier separation and transport efficiency, photocurrent and Electrochemical Impedance Spectroscopy (EIS) analyses were conducted. The photocurrent response in Figure 2a indicates that 0.050 CNT-NiCo₂S₄ showed the highest photocurrent density because of a much lower charge carrier recombination in 0.050C-NCS. The improved separation efficiency and lowest recombination rate of the photogenerated electron–hole pairs facilitated efficient photocatalytic reactions [57,58]. The photoreaction and separation of carriers are effective when the arc-radius of the EIS plot is less [59,60]. The EIS of the fabricated photocatalysts was analyzed to investigate the charge carriers' interface transfer/recombination efficiency. As can be seen from Figure 2b, 0.050C-NCS presented a much smaller arc size than the pure NiCo₂S₄, demonstrating that 0.050C-NCS had a lower electron transfer resistance and a positive effect on photo-induced carrier transfer. The Nyquist data of 0.050C-NCS were fitted with an equivalent circuit via Zview software (2.1.0.0) to determine the exact values of the R_{ESR} and R_{ct} resistances [61,62]. Figure S4 presents the fitted model of 0.050C-NCS with the most suitable modified Randle circuit model in the inset image. The value of the R_{ESR} and R_{ct} of the 0.050C-NCS sample electrode came to be 36.77 and 66.31 Ω , respectively. All of the above results demonstrate the excellent photocatalytic performance of 0.050C-NCS, consistent with the trend of the photocatalytic reduction results.

The effect of inorganic ions on photocatalytic activity has been reported in many studies. Among them, inorganic anions, such as NO_3^- , Cl^- , SO_4^{2-} , and PO_4^{3-} , may have two inhibitory effects: the first is the competitive adsorption of ions and pollutant molecules to the active sites on the TiO₂ surface, leading to a decrease in the photocatalytic efficiency. The second is that anions can react with the photogenerated holes, thus reducing the amount of oxides that degrade the pollutant molecules [12,63]. We investigated the effect of coexisting ions in the photocatalytic reduction process of Cr(VI). In Figure 3a, it is seen that the inhibition of the Cr(VI) reduction process was enhanced when the concentration of NaCl was gradually increased, which might have been due to the competition between chloride ions and Cr(VI) adsorption. Similarly, the addition of 10 mM of HCO_3^- and SO_4^{2-} to the solution had a relatively strong inhibitory effect on the reduction process of Cr(VI) (Figure 3b). The effect of cations on the reduction process of Cr(VI) was investigated in Figure 3c, from which it can be seen that the addition of Cu^{2+} significantly improved the

photocatalytic reduction rate of Cr(VI). This is because the positively charged Cu^{2+} was more likely to capture the electrons generated by photoexcitation on the catalyst surface than the negatively charged $\text{Cr}_2\text{O}_7^{2-}$, and Cu^{2+} was preferentially reduced to Cu^+ . At the same time, Cu^+ could rapidly undergo redox reactions with $\text{Cr}_2\text{O}_7^{2-}$, with $\text{Cr}_2\text{O}_7^{2-}$ being reduced to Cr^{3+} and Cu^+ being oxidized to Cu^{2+} . Since Cu^{2+} could capture the electrons generated on the catalyst surface faster than $\text{Cr}_2\text{O}_7^{2-}$, the recombination rate of the electron-hole pairs on the catalyst surface was significantly reduced, which resulted in a higher utilization of electrons on the catalyst surface. Therefore, a significant enhancement in the photocatalytic reduction rate occurred when a small amount of Cu^{2+} was added to the reaction system. The above process shows that Cu^{2+} plays a catalytic role in the photocatalytic reduction process of Cr(VI). As shown in the figure, the presence of cations such as Mg^{2+} , Ca^{2+} , K^+ , and Na^+ in the solution will reduce the reduction efficiency of Cr(VI). This inhibitory effect is mainly because these ions can quickly get the photoexcited electrons on the semiconductor conduction band, thus competing with Cr(VI) for electrons, inevitably reducing the reduction efficiency.

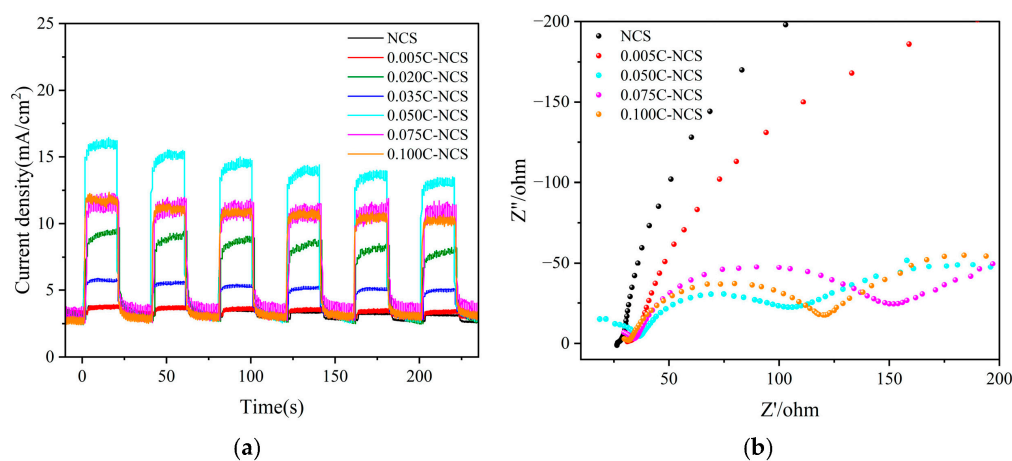


Figure 2. (a) Transient photocurrent responses of the as-prepared samples; and (b) electrochemical impedance spectra (EIS) of the as-prepared samples.

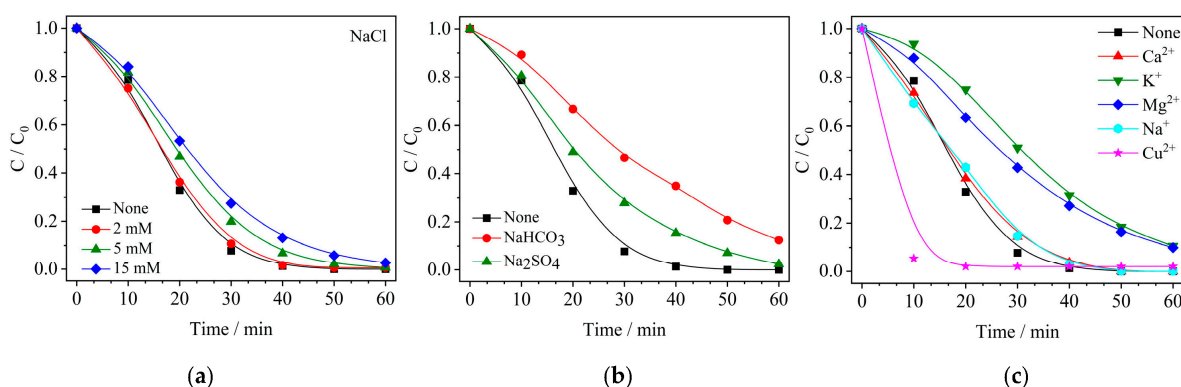


Figure 3. Photocatalytic reduction curves of Cr(VI) solution containing different concentrations of NaCl (a); and (b) sodium salts (10 mM) and (c) inorganic salts (10 mM).

3.2. Structural and Morphological Analysis

The X-ray diffraction (XRD) results of the NiCo_2S_4 with different MWCNT contents are shown in Figure 4. For the samples, eleven diffraction spikes were recorded at 26.8° , 31.6° , 33.0° , 38.3° , 47.4° , 50.5° , 55.3° , 58.1° , 62.5° , 65.1° , and 69.3° , respectively, indexed as 022, 031, 222, 040, 242, 511, 044, 253, 620, 053, and 244 using JCPDS No. 20-0782 [64]. It can be clearly seen from the image that the diffraction peaks of these as-prepared composites were relatively narrow and independent, indicating that the composites exhibited a better

crystalline state. However, no prominent diffraction peaks of the MWCNTs were observed, indicating that they were highly dispersed in the composites. With the introduction of MWCNTs, the NiCo_2S_4 was relatively dispersed, and the peak intensity decreased. The change in grain size can be reflected in the peak width of the diffraction peak [65]. It can be seen from the graph that the grain size of the pure NiCo_2S_4 was slightly larger. Furthermore, the grain sizes of the NiCo_2S_4 , 0.020C-NCS, 0.050C-NCS, and 0.100C-NCS photocatalysts were further calculated to be 321, 262, 136, and 148 nm, respectively, by using the Debye–Scherrer method [66,67]:

$$D = k\lambda/\beta \cos \theta$$

The photocatalytic activity generally increased with a decrease in the grain size [68]. The larger grain size of NiCo_2S_4 indicated that the photocatalytic reduction reaction of Cr(VI) with the pure NiCo_2S_4 had poor performance. The previous experimental results of photocatalytic reduction also confirmed this conclusion.

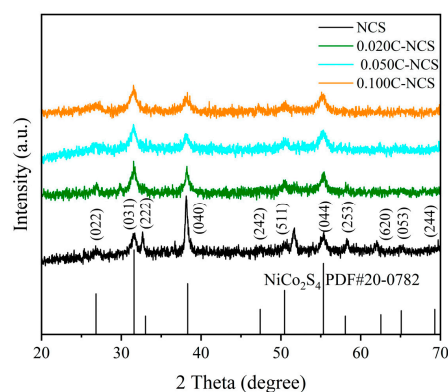


Figure 4. XRD pattern of as-prepared samples.

The structure and morphology of 0.050C-NCS were further characterized using SEM and TEM, as shown in Figure 5. From the SEM of 0.050C-NCS (Figure 5a,b), there were a large number of NiCo_2S_4 nanoparticles clustered on the surface of the carbon nanotubes. The appearance of the carrier MWCNTs and nanoparticle shape of NiCo_2S_4 proved that the NiCo_2S_4 nanoparticles were successfully loaded on the MWCNTs via hydrothermal synthesis. The nanostructure of 0.050C-NCS was further characterized using transmission electron microscopy (TEM), as shown in Figure 5c. The results of the TEM further observed that the morphology of 0.050C-NCS showed an apparent hollow tubular structure. In the high-resolution TEM (HR-TEM) image of 0.050C-NCS, it exhibits an ordered lattice structure (Figure 5d). The measured lattice fringe spacing between two adjacent planes was 0.27 nm, which matched well with the (222) lattice plane of NiCo_2S_4 , indicating the successful synthesis of NiCo_2S_4 materials. In addition, the element distribution of 0.050C-NCS (Figure 5e) was tested using SEM-EDS. The result showed that 0.050C-NCS comprised Ni in a light blue color, Co in a green color, S in a yellow color, C in a blue color, and N in red color, indicating the successful synthesis of 0.050C-NCS. Additionally, the Energy dispersive spectroscopy of 0.050 CNT- NiCo_2S_4 is presented in Figure S5.

3.3. Nitrogen Adsorption–Desorption Experiment

The specific surface area of photocatalysts is one of the critical factors affecting the performance of catalysts. The higher the specific surface area, the more reaction sites of the catalyst, which is beneficial to enhancing the photocatalytic performance of the catalyst. We can obtain the type of BET isotherm from the four informative sections of the BET plot: initial steepness, rounded knee, plateau, and final steepness. The prepared photocatalyst's BET isotherm (Figure 6 or Figures S6–S8) was of type II, as it had a low saturation pressure, an extended plateaus, and an almost vertical rise at a higher relative

pressure, which expresses the presence of a macro-sized pore. The higher the relative pressure, the more adsorption occurs, so the interaction between the adsorbent and the adsorbate is relatively weak. The photocatalyst's hysteresis was H3 type (slit-type pores) that almost diffused or overlapped with the adsorption curve, expressing the simple adsorption on and desorption from the surface [69]. The H3 hysteresis loops and III-type isotherms proved the mesoporous nature of the catalysts, and the pore size ranges counted in Table 1 were all within the mesoporous range. The specific surface area (S_{BET}), pore volume, and pore size of the prepared samples are presented in Table 1. The S_{BET} of the samples gradually increased with an increase in the MWCNT addition. Among them, the S_{BET} and pore volume of 0.050C-NCS increased to some extent compared to the pure $NiCo_2S_4$, which might have been due to the doping of MWCNTs inhibiting the crystallinity of $NiCo_2S_4$, resulting in a decrease in the grain size, thus increasing the S_{BET} and pore volume. Increasing the pore volume and S_{BET} of photocatalysts could provide more reaction sites for reducing Cr(VI). However, too much MWCNT addition will lead to the encapsulation of $NiCo_2S_4$ by the MWCNTs, reducing the photocatalytic performance.

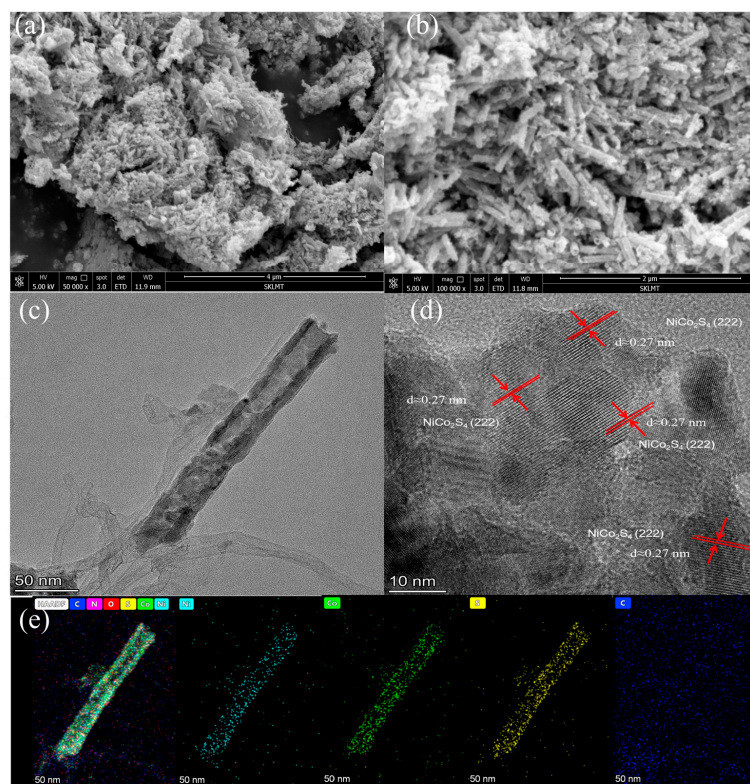


Figure 5. (a,b) SEM images, (c) TEM images, and (d) HRTEM images of 0.050C-NCS. (e) Elemental mapping of 0.050C-NCS.

Table 1. The BET parameters of the samples.

Sample	S_{BET} (m^2/g)	Pore Size (nm)	Pore Volume (cm^3/g)
NCS	16	34	0.133
0.005C-NCS	22	27	0.145
0.020C-NCS	51	22	0.290
0.035C-NCS	71	18	0.328
0.050C-NCS	91	20	0.460
0.075C-NCS	100	18	0.439
0.100C-NCS	125	15	0.467

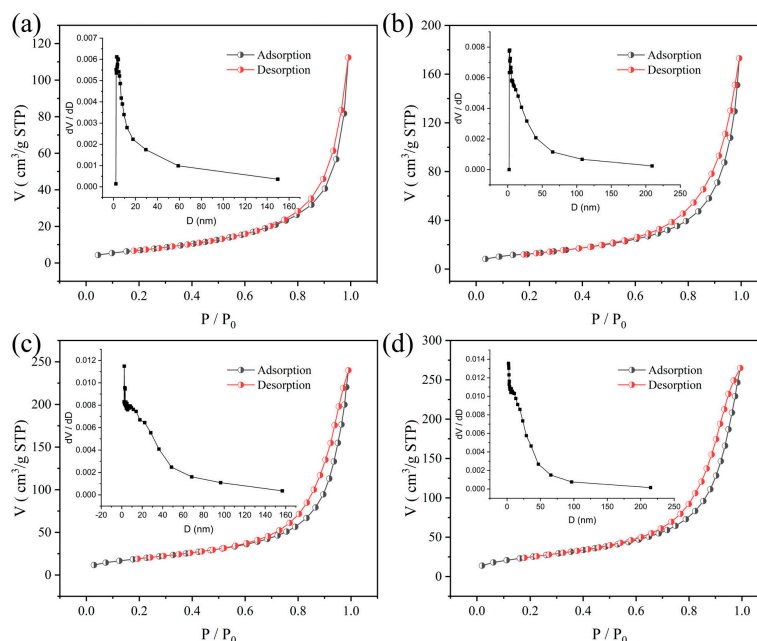


Figure 6. N₂ adsorption and desorption isotherms and corresponding pore-size distribution curves (inset) for (a) C-NCS; (b) 0.020C-NCS; (c) 0.050C-NCS; and (d) 0.100C-NCS.

3.4. Composition and Band Structure Analysis

To further determine the chemical compositions of the elements in the samples, 0.050C-NCS was characterized using X-ray photoelectron spectroscopy (XPS), and the results are shown in Figure 7. The peak positions of C, Ni, Co, S, N, and O can be observed in the survey spectra of Figure 7a, and the distribution of each element was relatively uniform. Specifically, the element N was present at a binding energy of 400 eV, and its content was relatively low. The absorption of some oxygen-containing substances in the air by the material might have caused the presence of the O 1s characteristic peak. As shown in Figure 7b, 0.050C-NCS showed two satellite peaks and two spin-orbit double peaks. The two spin-orbit double peaks were about 853.1 eV and 870 eV, corresponding to Ni²⁺, and the peaks were about 855.9 eV and 873.8 eV, corresponding to Ni³⁺, which proved the presence of Ni²⁺ and Ni³⁺ in 0.050C-NCS [58]. As shown in Figure 7c, in 0.050C-NCS, there were two spin-orbit double peaks at about 778.5 eV and 793.3 eV, corresponding to Co³⁺, and at about 797.3 eV and 781.08 eV, corresponding to Co²⁺. As shown in Figure 7d, the S 2p spectrum showed two peaks at 162.5 eV and 161.5 eV, attributed to S 2p_{1/2} and S 2p_{3/2}, which showed the valence state of S²⁻ [58]. The fractional peak at 163.5 eV was attributed to the metallic sulfur (M-S) in 0.050C-NCS, demonstrating the presence of the Ni-Co-S phase [63]. The other peak with a binding energy of 168.6 eV represented the oxidized S bond, meaning that some surface sulfide ions were oxidized during the XPS test. The C 1s spectrum was decomposed into three characteristic peaks at 288, 285.8, and 284.8 eV (Figure 7e), which could be attributed to the C=O/C=N, C-O/C-N, and C=C/C-C bonds, respectively [70,71]. From the N 1s spectra, the nitrogen atoms contained different oxidation states, including pyridine-N (398.4 eV), pyrrole-N (400.1 eV), and pyridine-N-oxide (402.2 eV) (Figure 7f) [72].

To investigate the band structure alignment of 0.050C-NCS, UV-Vis Diffuse Reflectance Absorption Spectra (DRS) were obtained, as shown in Figure 8. As shown in Figure 8a, 0.050C-NCS presented a clear absorption edge at around 485.2 nm. The optical energy gap was calculated by using the given equation: $\alpha h\nu = A(h\nu - E_g)^n$, where h , α , ν , A , and E_g are the equation parameters [73]. The bandgap energy of 0.050C-NCS was 2.56 eV (Figure 8b). Figure S9 shows that the absorption edge of the pure NiCo₂S₄ was at 417.2 nm. The light absorption of 0.050C-NCS showed a light red shift compared to the pure NiCo₂S₄, indicating that introducing MWCNTs enhanced the light absorption performance.

As shown in Figure 8c, the slope of the Mott–Schottky plot is positive, so 0.050C-NCS belonged to the n-type semiconductor. Generally, the flat band potential was close to the bottom of the conduction band of the n-type semiconductor. The flat band potential calculated from the x-intercept of the linear regions of this plot was -0.63 eV (vs. Ag/AgCl) for 0.050C-NCS (-0.43 eV, vs. NHE). The conduction band was smaller than the flat band by 0.2 eV. Thus, the conduction band of 0.050C-NCS was -0.63 eV (vs. NHE). According to the equation $E_{VB} = E_{CB} + E_g$ [74], the valence band position (E_{VB}) of 0.050C-NCS could be calculated as 1.93 eV. The relative band structure alignment of 0.050C-NCS is illustrated in Figure 8d. Also, the potential of $E_{Cr^{6+}(Cr_2O_7^{2-}/Cr^{3+})}$ could be calculated as 1.33 eV when the solution was acidic. Therefore, Cr(VI) can be easily reduced by the 0.050C-NCS photocatalyst system. Adding MWCNTs accelerated the charge transfer, which was more conducive to the reaction.

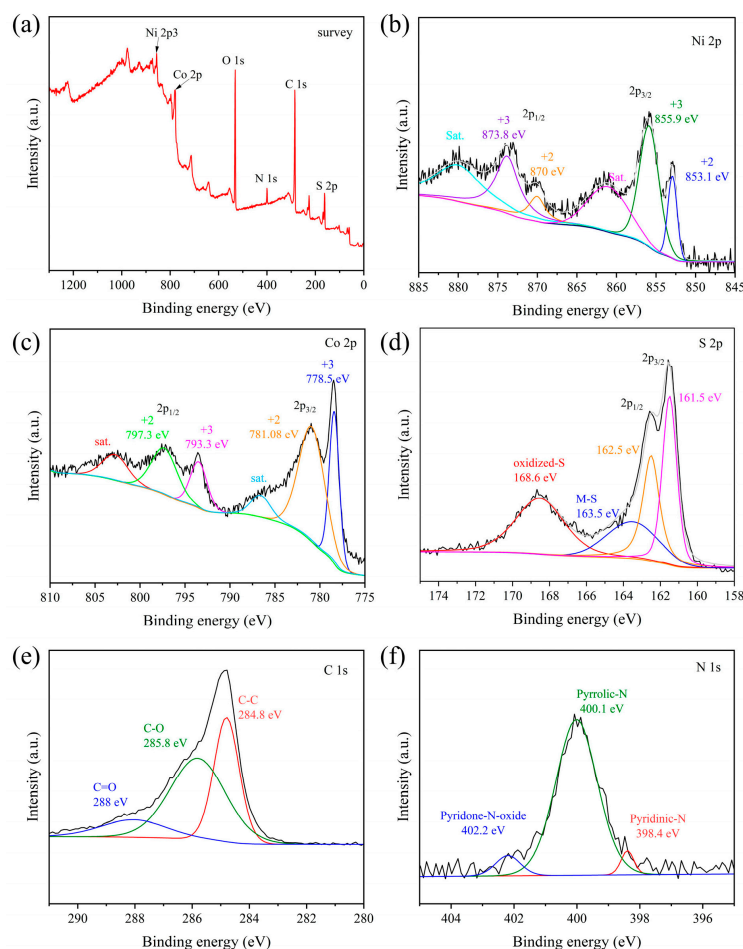


Figure 7. XPS survey spectra (a) and high-resolution XPS spectrum of 0.050C-NCS ((b) Ni 2p; (c) Co 2p; (d) S 2p; (e) C 1s; and (f) N 1s).

The results indicated that MWCNTs incorporated into $NiCo_2S_4$ nanoparticles improved the efficiency of visible light absorption and excitation separation. The high activity of 0.050C-NCS was attributed to the high charge transfer and low photoexcited electron–hole recombination properties. The good chemical and thermal stability, large surface area, and excellent mechanical properties of MWCNTs make them ideal as support materials for hybridization with photocatalysts for applications in modifying photocatalysts. When MWCNTs were hybridized with $NiCo_2S_4$, they not only exerted the advantage of inhibiting photocatalyst aggregation. Moreover, they also acted as a sink in the transfer of photogenerated electrons. In this photocatalyst system, MWCNTs acted as “electron sinks” to receive the photogenerated electrons from $NiCo_2S_4$, effectively separating the electron–hole pairs.

Thus, the recombination of photogenerated carriers was effectively suppressed. Moreover, the photogenerated electrons on MWCNT could participate in the photocatalytic reaction and effectively photocatalytically reduce Cr(VI) to Cr(III). In addition, the reaction equation for the photocatalytic reduction of Cr(VI) to Cr(III) is as follows [45]:

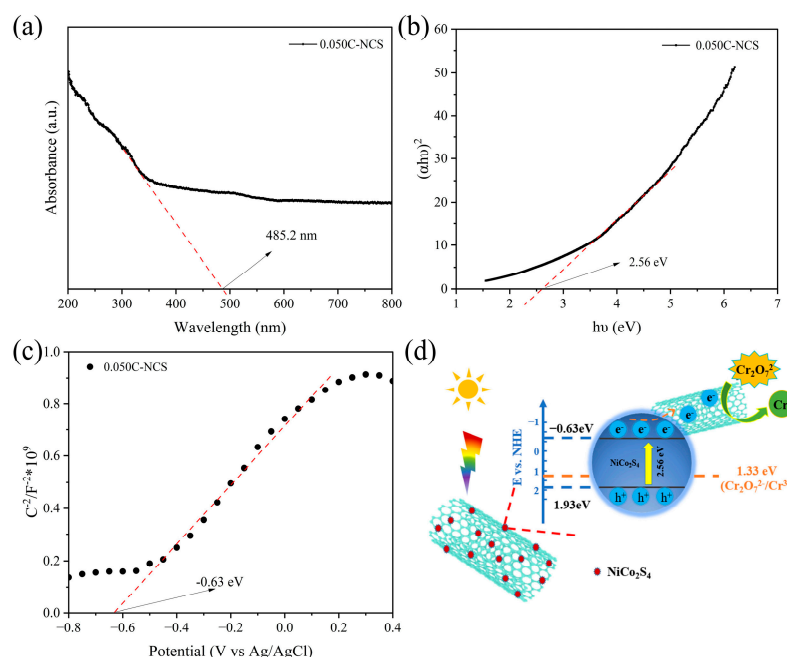
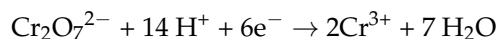


Figure 8. (a) UV-Vis Diffuse Reflectance Absorption Spectra (DRS); (b) direct band gap energy; (c) Mott–Schottky plots, and (d) schematic illustration of 0.050C-NCS.

3.5. Stability of the Catalyst

In addition, as a photocatalyst with an excellent performance, it should remain stable under repeated cycles. Cyclic photocatalytic experiments confirmed the stability of 0.050C-NCS. As shown in Figure 9, the results showed that 0.050C-NCS maintained a high reduction rate after being used five times. It maintained a 91.4% reduction rate in the fourth photocatalytic Cr(VI) reduction, while a sharp decrease occurred in the fifth cycle. In general, 0.050CNT-NiCo₂S₄ had a relatively good application for reducing Cr(VI) in the first four cycles.

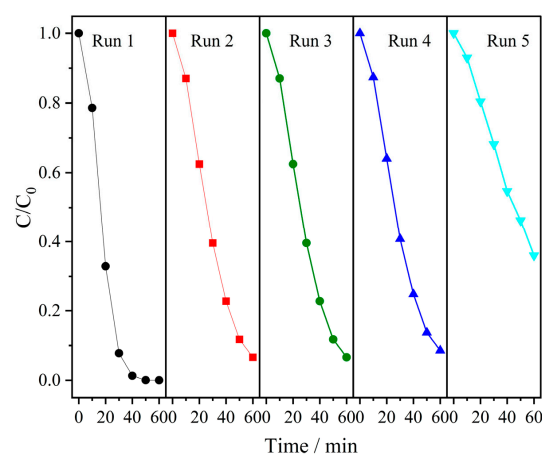


Figure 9. Stability of 0.050C-NCS within five consecutive cycles.

4. Conclusions

In summary, a facile two-step hydrothermal method was used to prepare CNT-NiCo₂S₄ composites with different MWCNT contents. The composite samples showed excellent photocatalytic activities with a good reduced Cr(VI) stability. The 0.050C-NCS sample could reduce Cr(VI) within 40 min, attributed to the large specific surface area, enhanced visible light absorption, and efficient separation and transport of photogenerated electron–hole pairs resulting from the MWCNT introduction. MWCNTs could receive photogenerated electrons from NiCo₂S₄ and effectively separate the photogenerated electron–hole pairs. Therefore, the recombination of photogenerated carriers was effectively suppressed. After the addition of MWCNTs, an improvement in the visible light absorption and carrier separation efficiency of NiCo₂S₄ was realized, and the photogenerated electrons on the MWCNTs could effectively photocatalytic reduce Cr(VI) to Cr(III). Therefore, the MWCNT-based composite photocatalyst could effectively reduce Cr(VI). This work's strategy for building a CNT-based photocatalyst provides a promising method for completely removing high-valence heavy metal ions.

Supplementary Materials: The following supporting information can be downloaded at: <https://www.mdpi.com/article/10.3390/c9040099/s1>. Figure S1: The schematic diagram of the reactor; Figure S2: ESR spectrum of the •O₂[−] produced by NiCo₂S₄ and 0.050 CNT-NiCo₂S₄ under visible-light irradiation; Figure S3: Effect of scavengers on photocatalytic degradation of Cr(VI) during the trapping experiments of the 0.050 CNT-NiCo₂S₄; Figure S4: Circuit fitted Nyquist plot of the 0.050C-NCS with a suitable modified Randle circuit (inset); Figure S5: Energy dispersive spectroscopy of 0.050 CNT-NiCo₂S₄; Figure S6: N₂ adsorption and desorption isotherms and corresponding pore-size distribution curves (inset) for 0.005 CNT-NiCo₂S₄; Figure S7: N₂ adsorption and desorption isotherms and corresponding pore-size distribution curves (inset) for 0.035 CNT-NiCo₂S₄; Figure S8: N₂ adsorption and desorption isotherms and corresponding pore-size distribution curves (inset) for 0.075 CNT-NiCo₂S₄; Figure S9: UV-Vis Diffuse Reflectance Absorption Spectra (DRS) of as-prepared samples with different amounts of CNT; Table S1: Comparison of photocatalytic efficiency for photocatalytic reduction of Cr(VI) between previously reported literature and the present work.

Author Contributions: Methodology, validation, formal analysis, writing—original draft, Q.J.; investigation, data curation, visualization, Y.F., S.T. and Z.Z.; writing—review and editing, conceptualization, supervision, funding acquisition, Z.H. All authors have read and agreed to the published version of the manuscript.

Funding: This research was funded by the Young Taishan Scholars Program of Shandong Province (no. tsqn.201909026), the Youth Interdisciplinary Science and Innovative Research Groups of Shandong University (no. 2020QNQT014), the Shandong University Future Youth Grant Program (no. 61440089964189).

Data Availability Statement: Data will be made available on request.

Acknowledgments: The authors thank Sen Wang from State Key Laboratory of Microbial Technology of Shandong University for assisting with SEM analysis.

Conflicts of Interest: The authors declare that they have no known competing financial interests or personal relationships that could have appeared to influence the work reported in this paper.

References

1. Li, J.; You, J.; Wang, Z.; Zhao, Y.; Xu, J.; Li, X.; Zhang, H. Application of alpha-Fe₂O₃-based heterogeneous photo-fenton catalyst in wastewater treatment: A review of recent advances. *J. Environ. Chem. Eng.* **2022**, *10*, 108329. [[CrossRef](#)]
2. Li, S.; Cai, M.; Wang, C.; Liu, Y.; Li, N.; Zhang, P.; Li, X. Rationally designed Ta₃N₅/BiOCl S-scheme heterojunction with oxygen vacancies for elimination of tetracycline antibiotic and Cr(VI): Performance, toxicity evaluation and mechanism insight. *J. Mater. Sci. Technol.* **2022**, *123*, 177–190. [[CrossRef](#)]
3. Kholisa, B.; Matsena, M.; Chirwa, E.M.N. Evaluation of Cr(VI) reduction using indigenous bacterial consortium isolated from a municipal wastewater sludge: Batch and kinetic studies. *Catalysts* **2021**, *11*, 1100. [[CrossRef](#)]
4. Cheng, L.; He, R.L.; Min, D.; Li, W.W.; Liu, D.F.; Yu, H.Q. Engineering a rhamnose-inducible system to enhance the extracellular electron transfer ability of *Shewanella* genus for improved Cr(VI) reduction. *ACS EST Eng.* **2021**, *1*, 842–850. [[CrossRef](#)]

5. Jin, Q.; Dai, M.; Zhan, X.; Wang, S.; He, Z. Carbon nanotubes and graphene composites used in Cr(VI) detection techniques: A review. *J. Alloys Compd.* **2022**, *922*, 166268. [[CrossRef](#)]
6. Djouider, F. Radiolytic formation of non-toxic Cr(III) from toxic Cr(VI) in formate containing aqueous solutions: A system for water treatment. *J. Hazard. Mater.* **2012**, *223*, 104–109. [[CrossRef](#)] [[PubMed](#)]
7. Meinhold, V.; Hoehlich, D.; Mehner, T.; Lampke, T. Electrodeposition of thick and crack-free Fe-Cr-Ni coatings from a Cr (III) electrolyte. *Coatings* **2022**, *12*, 56. [[CrossRef](#)]
8. Qi, Y.; Jiang, M.; Cui, Y.-L.; Zhao, L.; Liu, S. Novel reduction of Cr(VI) from wastewater using a naturally derived microcapsule loaded with rutin-Cr(III) complex. *J. Hazard. Mater.* **2015**, *285*, 336–345. [[CrossRef](#)]
9. Xu, J.-J.; Gu, H.-Y.; Chen, M.-D.; Li, X.-P.; Zhao, H.-W.; Yang, H.-B. Dual Z-scheme Bi₃TaO₇/Bi₂S₃/SnS₂ photocatalyst with high performance for Cr(VI) reduction and TC degradation under visible light irradiation. *Rare Metals* **2022**, *41*, 2417–2428. [[CrossRef](#)]
10. Qin, C.; Pan, G.; Zhang, Y.; Ding, F.; Qu, J.; Xu, X.; Su, X. Efficient reduction of Cr (VI) to Cr (III) over a TiO₂-supported palladium catalyst using formic acid as a reductant. *Catalysts* **2022**, *12*, 179. [[CrossRef](#)]
11. Zhang, T.; Pan, Z.L.; Song, D.G.; Huang, H.; Yu, J.; Wen, Y.C.; Lu, J.L.; Bian, Z.F.; Qian, X.F. Interstitial compound Fe₃C-soped Fe(0) nanoparticles embedded in mesoporous carbon boosting Cr(VI) removal. *ACS EST Eng.* **2022**, *3*, 131–137. [[CrossRef](#)]
12. Yang, D.Z.; Chu, Z.T.; Feng, X.Z.; Ge, Q.Y.; Wang, R.H.; Zhang, J.; Li, S.Y.; Zheng, R.J.; Wei, W.F.; Yi, S.P.; et al. Dual ions neutralized and stabilized red mud for chromium(VI) polluted soil remediation. *ACS EST Eng.* **2022**, *2*, 913–923. [[CrossRef](#)]
13. Zarras, P.; Miller, C.E.; Webber, C.; Anderson, N.; Stenger-Smith, J.D. Laboratory and field studies of Poly(2,5-bis(N-methyl-N-hexylamino)phenylene vinylene) (BAM-PPV): A potential wash primer replacement for army military vehicles. *Coatings* **2014**, *4*, 687–700. [[CrossRef](#)]
14. Gao, Y.; Yang, X.; Lu, X.; Li, M.; Wang, L.; Wang, Y. Kinetics and mechanisms of Cr(VI) removal by nZVI: Influencing parameters and modification. *Catalysts* **2022**, *12*, 999. [[CrossRef](#)]
15. Gao, Y.; Sun, W.; Yang, W.; Li, Q. Palladium nanoparticles supported on amine-functionalized glass fiber mat for fixed-bed reactors on the effective removal of hexavalent chromium by catalytic reduction. *J. Mater. Sci. Technol.* **2018**, *34*, 961–968. [[CrossRef](#)]
16. Shang, H.; Zhang, S.; Zhu, X. Biomass cellulose component and Fe mineral catalysis help Cr(VI) to realize almost 100% pyrolysis reduction efficiency. *ACS EST Eng.* **2021**, *1*, 1441–1448. [[CrossRef](#)]
17. Vaddi, D.R.; Gurugubelli, T.R.; Koutavarapu, R.; Lee, D.-Y.; Shim, J. Bio-stimulated adsorption of Cr(VI) from aqueous solution by groundnut shell activated carbon@Al embedded material. *Catalysts* **2022**, *12*, 290. [[CrossRef](#)]
18. Rahmat, S.T.; Alias, N.; Kumar, R.; Tan, W.K.; Kawamura, G.; Matsuda, A.; Lockman, Z. Electrophoretic deposition of graphene oxide and reduced graphene oxide on the rutile phase of TiO₂ nanowires for rapid reduction of Cr (VI) under simulated sunlight irradiation. *Catalysts* **2022**, *12*, 1282. [[CrossRef](#)]
19. Wan, Z.; Mao, Q.; Xiang, J.; Ma, D.; Tang, H. Greatly increased visible-light photocatalytic activity of SnS₂/carbon nanotube composite for Cr(VI) reduction: Insights into effects of solid acid structure. *J. Mater. Sci. Technol.* **2023**, *161*, 233–244. [[CrossRef](#)]
20. Yu, M.D.; Mao, X.H.; He, X.S.; Zheng, M.X.; Meng, Y.; He, F.; Xi, B.D. Enhanced sequestration of chromium by mechanochemically silicified microscale zerovalent iron: Role of the silicate-modified surface. *ACS EST Eng.* **2023**, *3*, 1604–1613. [[CrossRef](#)]
21. Asimakopoulos, G.; Karakassides, A.; Baikousi, M.; Gioti, C.; Moschovas, D.; Avgeropoulos, A.; Bourlinos, A.B.; Douvalis, A.P.; Salmas, C.E.; Karakassides, M.A. Nanoporous carbon magnetic hybrid derived from waterlock polymers and its application for hexavalent chromium removal from aqueous solution. *C-J. Carbon Res.* **2021**, *7*, 69. [[CrossRef](#)]
22. Smith, V.A.; Rivera, J.F.A.; Bello, R.; Rodriguez-Aguado, E.; Elshaer, M.R.; Wodzinski, R.L.; Bashkova, S. The role of surface chemistry and polyethylenimine grafting in the removal of Cr (VI) by activated carbons from cashew nut shells. *C-J. Carbon Res.* **2021**, *7*, 27. [[CrossRef](#)]
23. Feng, H.-F.; Yu, Y.-X.; Jiang, S.-Q.; Shang, J.; Cheng, Y.; Wang, L.; Hao, W.-C.; Wang, T.-M. Synthesis of magnetic core-shell iron nanochains for potential applications in Cr(VI) ion pollution treatment. *Rare Metals* **2021**, *40*, 176–179. [[CrossRef](#)]
24. Zhou, H.; Chen, Y. Effect of acidic surface functional groups on Cr(VI) removal by activated carbon from aqueous solution. *Rare Metals* **2010**, *29*, 333–338. [[CrossRef](#)]
25. Yu, J.X.; Fu, Q.; Yang, H.S.; Ouyang, G.F.; Wang, J.H.; Hao, Z.P. Synergistic catalytic organic pollutants degradation and Cr(VI) reduction by carbon nanotubes through an electron-transfer mechanism without external energy or chemical input. *ACS EST Eng.* **2022**, *2*, 1221–1228. [[CrossRef](#)]
26. Mu, F.H.; Dai, B.L.; Zhao, W.; Zhou, S.J.; Huang, H.B.; Yang, G.; Xia, D.H.; Kong, Y.; Leung, D.Y.C. Construction of a novel Ag/Ag₃PO₄/MIL-68(In)-NH₂ plasmonic heterojunction photocatalyst for high-efficiency photocatalysis. *J. Mater. Sci. Technol.* **2022**, *101*, 37–48. [[CrossRef](#)]
27. Xiong, J.; Zeng, H.Y.; Xu, S.; Peng, J.F.; Liu, F.Y.; Wang, L.H. Enhancing the intrinsic properties of flower-like BiOI by S-doping toward excellent photocatalytic performances. *J. Mater. Sci. Technol.* **2022**, *118*, 181–189. [[CrossRef](#)]
28. Zhang, M.; Zhao, X.; Dong, Y.; Hu, C.; Xiang, X.; Zeng, X.; Jia, J.; Jin, C.; Ding, L.; Chen, X. In-situ synthesis of 0D/1D CeO₂/Zn_{0.4}Cd_{0.6}S S-scheme heterostructures for boosting photocatalytic remove of antibiotic and chromium. *Ceram. Int.* **2023**, *49*, 5842–5853. [[CrossRef](#)]
29. Zhang, M.; Dong, Y.; Peng, M.; Chen, X.; Zheng, Q.; Liao, J.; Chen, W. Band gap-controllable N, P co-doped carbon@Zn_xCd_{1-x}In₂S₄ for photocatalytic reduction of chromium(VI) and degradation of tetracycline hydrochloride. *Sep. Purif. Technol.* **2023**, *322*, 124294. [[CrossRef](#)]

30. Shearer, C.J.; Alvino, J.F.; Batmunkh, M.; Metha, G.E. Pt nanocluster co-catalysts for photocatalytic water splitting. *C-J. Carbon Res.* **2018**, *4*, 64. [[CrossRef](#)]
31. Ratova, M.; Sawtell, D.; Kelly, P.J. Micro-patterning of magnetron sputtered titanium dioxide coatings and their efficiency for photocatalytic applications. *Coatings* **2020**, *10*, 68. [[CrossRef](#)]
32. Roveri, M.; Goidanich, S.; Toniolo, L. Artificial ageing of photocatalytic nanocomposites for the protection of natural stones. *Coatings* **2020**, *10*, 729. [[CrossRef](#)]
33. Shen, R.; Hao, L.; Chen, Q.; Zheng, Q.; Zhang, P.; Li, X. P-Doped g-C₃N₄ nanosheets with highly dispersed Co_{0.2}Ni_{1.6}Fe_{0.2}P cocatalyst for efficient photocatalytic hydrogen evolution. *Acta Phys.-Chim. Sin.* **2022**, *38*, 2110014.
34. Saleh, T.S.; Badawi, A.K.; Salama, R.S.; Mostafa, M.M.M. Design and development of novel composites containing nickel ferrites supported on activated carbon derived from agricultural wastes and its application in water remediation. *Materials* **2023**, *16*, 2170. [[CrossRef](#)]
35. Raditoiu, V.; Raditoiu, A.; Raduly, M.F.; Amariutei, V.; Gifu, I.C.; Anastasescu, M. Photocatalytic behavior of water-based styrene-acrylic coatings containing TiO₂ sensitized with metal-phthalocyanine tetracarboxylic acids. *Coatings* **2017**, *7*, 229. [[CrossRef](#)]
36. Huang, G.Q.; Ye, W.N.; Lv, C.X.; Butenko, D.S.; Yang, C.; Zhang, G.L.; Lu, P.; Xu, Y.; Zhang, S.C.; Wang, H.W.; et al. Hierarchical red phosphorus incorporated TiO₂ hollow sphere heterojunctions toward superior photocatalytic hydrogen production. *J. Mater. Sci. Technol.* **2022**, *108*, 18–25. [[CrossRef](#)]
37. Zhu, H.; Tan, J.; Qiu, J.; Wang, D.; Zhao, Z.; Lu, Z.; Huang, G.; Liu, X.; Mei, Y. Gold nanoparticles decorated titanium oxide nanotubes with enhanced antibacterial activity driven by photocatalytic memory effect. *Coatings* **2022**, *12*, 1351. [[CrossRef](#)]
38. Alasri, T.M.; Ali, S.L.; Salama, R.S.; Alshorifi, F.T. Band-structure engineering of TiO₂ photocatalyst by AuSe quantum dots for efficient degradation of malachite green and phenol. *J. Inorg. Organomet. Polym. Mater.* **2023**, *33*, 1729–1740. [[CrossRef](#)]
39. Zhang, S.J.; He, Z.L.; Xu, S.S.; Li, X.; Zhang, J.; Zhan, X.P.; Dai, M.; Wang, S.G. In situ liquid-phase growth strategies of g-C₃N₄ solar-driven heterogeneous catalysts for environmental applications. *Sol. RRL* **2021**, *5*, 2100233. [[CrossRef](#)]
40. Jin, Z.; Li, Y.; Hao, X. Ni, Co-based selenide anchored g-C₃N₄ for boosting photocatalytic hydrogen evolution. *Acta Phys.-Chim. Sin.* **2021**, *37*, 1912033.
41. Fernandez-Catala, J.; Greco, R.; Navlani-Garcia, M.; Cao, W.; Berenguer-Murcia, A.; Cazorla-Amoros, D. g-C₃N₄-based direct Z-scheme photocatalysts for environmental applications. *Catalysts* **2022**, *12*, 1137. [[CrossRef](#)]
42. Dai, M.; Yu, H.; Chen, W.; Qu, K.-A.; Zhai, D.; Liu, C.; Zhao, S.; Wang, S.; He, Z. Boosting photocatalytic activity of CdLa₂S₄/ZnIn₂S₄ S-scheme heterojunctions with spatial separation of photoexcited carries. *Chem. Eng. J.* **2023**, *470*, 144240. [[CrossRef](#)]
43. Xiong, Z.; Hou, Y.; Yuan, R.; Ding, Z.; Ong, W.-J.; Wang, S. Hollow NiCo₂S₄ Nanospheres as a cocatalyst to support ZnIn₂S₄ nanosheets for visible-light-driven hydrogen production. *Acta Phys.-Chim. Sin.* **2022**, *38*, 2111021.
44. Zeng, J.-Y.; Wang, X.-S.; Xie, B.-R.; Li, Q.-R.; Zhang, X.-Z. Large pi-conjugated metal-organic frameworks for infrared-light-driven CO₂ reduction. *J. Am. Chem. Soc.* **2022**, *144*, 1218–1231. [[CrossRef](#)]
45. Lan, C.; Meng, L.; Xu, N. One-pot synthesis of the direct Z-scheme AgInS₂/AgIn₅S₈ QDs heterojunction for efficient photocatalytic reduction of Cr⁶⁺ in neutral condition. *Colloids Surf. A Physicochem. Eng. Asp.* **2022**, *632*, 127762. [[CrossRef](#)]
46. Dai, M.; He, Z.; Zhang, P.; Li, X.; Wang, S. ZnWO₄-ZnIn₂S₄ S-scheme heterojunction for enhanced photocatalytic H₂ evolution. *J. Mater. Sci. Technol.* **2022**, *122*, 231–242. [[CrossRef](#)]
47. He, Z.; Byun, J.-H.; Zhou, G.; Park, B.-J.; Kim, T.-H.; Lee, S.-B.; Yi, J.-W.; Um, M.-K.; Chou, T.-W. Effect of MWCNT content on the mechanical and strain-sensing performance of thermoplastic polyurethane composite fibers. *Carbon* **2019**, *146*, 701–708. [[CrossRef](#)]
48. He, Z.; Zhou, G.; Byun, J.H.; Lee, S.K.; Um, M.K.; Park, B.; Kim, T.; Lee, S.B.; Chou, T.W. Highly stretchable multi-walled carbon nanotube/thermoplastic polyurethane composite fibers for ultrasensitive, wearable strain sensors. *Nanoscale* **2019**, *11*, 5884–5890. [[CrossRef](#)]
49. Zhang, S.; Zhang, N.; Zhang, J. Controlled synthesis of carbon nanotubes: Past, present and future. *Acta Phys.-Chim. Sin.* **2020**, *36*, 1907021. [[CrossRef](#)]
50. Adusei, P.K.; Johnson, K.; Kanakaraj, S.N.; Zhang, G.; Fang, Y.; Hsieh, Y.-Y.; Khosravifar, M.; Gbordzoe, S.; Nichols, M.; Shanov, V. Asymmetric fiber supercapacitors based on a FeC₂O₄/FeOOH-CNT hybrid material. *C-J. Carbon Res.* **2021**, *7*, 62. [[CrossRef](#)]
51. Zhang, J.; Dai, M.; Zhang, S.; Dai, M.; Zhang, P.; Wang, S.; He, Z. Recent progress on carbon-nanotube-based materials for photocatalytic applications: A review. *Sol. RRL* **2022**, *6*, 2200243. [[CrossRef](#)]
52. Liu, S.-Q.; Wang, S.; Dai, G.-P.; Lu, J.; Liu, K. Enhanced visible-light photocatalytic activity and stability of nano-sized Ag₂CO₃ combined with carbon nanotubes. *Acta Phys.-Chim. Sin.* **2014**, *30*, 2121–2126.
53. Toloman, D.; Stefan, M.; Macavei, S.; Barbu-Tudoran, L.; Popa, A. Photocatalytic self-cleaning PVDF membrane blended with MWCNT-ZnO nanocomposites for RhB removal. *Coatings* **2023**, *13*, 594. [[CrossRef](#)]
54. Miklec, K.; Grcic, I.; Radetic, L.; Cingesar, I.K.; Vrsaljko, D. Photocatalytic oxidation of amoxicillin in CPC reactor over 3D printed TiO₂-CNT@PETG static mixers. *Coatings* **2023**, *13*, 386. [[CrossRef](#)]
55. Gomis-Berenguer, A.; Iniesta, J.; Fermin, D.J.; Ania, C.O. Photoelectrochemical response of WO₃/nanoporous carbon anodes for photocatalytic water oxidation. *C-J. Carbon Res.* **2018**, *4*, 45. [[CrossRef](#)]

56. Falara, P.P.; Ibrahim, I.; Zourou, A.; Sygellou, L.; Sanchez, D.E.; Romanos, G.E.; Givalou, L.; Antoniadou, M.; Arfanis, M.K.; Han, C.; et al. Bi-functional photocatalytic heterostructures combining titania thin films with carbon quantum dots (C-QDs/TiO₂) for effective elimination of water pollutants. *Environ. Sci. Pollut. Res.* **2023**. [[CrossRef](#)]
57. Bai, S.; Li, X.; Kong, Q.; Long, R.; Wang, C.; Jiang, J.; Xiong, Y. Toward enhanced photocatalytic oxygen evolution: Synergistic utilization of plasmonic effect and Schottky junction via interfacing facet selection. *Adv. Mater.* **2015**, *27*, 3444–3452. [[CrossRef](#)]
58. Yuan, K.; Gao, T.-J.; Yang, Y.; Luo, W.; Li, S.; Zhang, C.-Y.; Xu, J.-X.; Li, N.; Zhu, Y.-R. Template sacrificial controlled synthesis of hierarchical nanoporous carbon@NiCo₂S₄ microspheres for high-performance hybrid supercapacitors. *Rare Metals* **2023**, *42*, 2643–2657. [[CrossRef](#)]
59. Rashid, M.; Hassan, W.; Aadil, M.; Somaily, H.H.; Mahdi, N.M.; Lataef, R.; Taki, A.G.; Srithilat, K.; Baamer, D.F.; Albukhari, S.M.; et al. Solar-light-driven and magnetically recoverable doped nano-ferrite: An ideal photocatalyst for water purification applications. *Opt. Mater.* **2023**, *135*, 113192. [[CrossRef](#)]
60. Nazik, G.; Aadil, M.; Zulfiqar, S.; Hassan, W.; Rahman, A.; Ibrahim, S.M.; Naseem, K.; Sheikh, T.A.; Akhtar, M.N. Synthesis of doped metal sulfide nanoparticles and their graphene reinforced nanohybrid for Pb(II) detection. *Z. Für Phys. Chem.* **2023**, *237*, 1257–1285. [[CrossRef](#)]
61. Aadil, M.; Zulfiqar, S.; Agboola, P.O.; Aboud, M.F.A.; Shakir, I.; Warsi, M.F. Fabrication of graphene supported binary nanohybrid with multiple approaches for electrochemical energy storage applications. *Synth. Met.* **2021**, *272*, 116645. [[CrossRef](#)]
62. Tariq, R.; Zulfiqar, S.; Somaily, H.H.; Warsi, M.F.; Ayman, I.; Hanif, F.; Akhtar, M.; Aadil, M. Synthesis of carbon supported iron oxide nanochips and their composite with glutathione: A novel electrochemical sensitive material. *Surf. Interfaces* **2022**, *34*, 102350. [[CrossRef](#)]
63. Dai, M.; He, Z.; Cao, W.; Zhang, J.; Chen, W.; Jin, Q.; Que, W.; Wang, S. Rational construction of S-scheme BN/MXene/ZnIn₂S₄ heterojunction with interface engineering for efficient photocatalytic hydrogen production and chlorophenols degradation. *Sep. Purif. Technol.* **2023**, *309*, 123004. [[CrossRef](#)]
64. Guo, M.-L.; Wu, Z.-Y.; Zhang, M.-M.; Huang, Z.-J.; Zhang, K.-X.; Wang, B.-R.; Tu, J.-C. Coupling interface constructions of FeOOH/NiCo₂S₄ by microwave-assisted method for efficient oxygen evolution reaction. *Rare Metals* **2023**, *42*, 1847–1857. [[CrossRef](#)]
65. Aadil, M.; Hassan, W.; Somaily, H.H.; Ejaz, S.R.; Abass, R.R.; Jasem, H.; Hachim, S.K.; Adhab, A.H.; Abood, E.S.; Alsafari, I.A. Synergistic effect of doping and nanotechnology to fabricate highly efficient photocatalyst for environmental remediation. *J. Alloys Compd.* **2022**, *920*, 165876. [[CrossRef](#)]
66. Tamam, N.; Aadil, M.; Hassan, W.; Ejaz, S.R.; Najm, Z.M.; Alsafari, I.A.; Aman, S.; Trukhanov, A.V.; Al-Buriah, M.S.; Boukhris, I. Surfactant assisted synthesis of nanostructured Mn-doped CuO: An efficient photocatalyst for environmental remediation. *Ceram. Int.* **2022**, *48*, 29589–29600. [[CrossRef](#)]
67. Ishfaq, M.; Aadil, M.; Ejaz, S.R.; Hassan, W.; Panduro-Tenazoa, N.M.; El Sayed, M.E.; Murshed, M.N.; El-Bahy, Z.M. Synthesis of binary metal doped CeO₂ via the subcritical hydrothermal method for photo-mineralizing methyl orange dye. *J. Alloys Compd.* **2023**, *960*, 170661. [[CrossRef](#)]
68. Badovinac, I.J.; Peter, R.; Omerzu, A.; Salamon, K.; Saric, I.; Samarzija, A.; Percic, M.; Piltaver, I.K.; Ambrozic, G.; Petravic, M. Grain size effect on photocatalytic activity of TiO₂ thin films grown by atomic layer deposition. *Thin Solid Films* **2020**, *709*, 138215. [[CrossRef](#)]
69. Li, T.; Aadil, M.; Zulfiqar, S.; Anwar, A.; Yakout, S.M.; Panduro-Tenazoa, N.M.; Mubeen, S. Synthesis of doped and porous CuO with boosted light-harvesting features for the photocatalytic mineralization of azo dyes. *Ceram. Int.* **2023**, *49*, 27827–27836. [[CrossRef](#)]
70. Bai, Y.; Xu, S.; Chen, J.; Sun, X.; Zhao, S.; Chang, J.; He, Z. Ti₃C₂@g-C₃N₄/TiO₂ ternary heterogeneous photocatalyst for promoted photocatalytic degradation activities. *Coatings* **2023**, *13*, 655. [[CrossRef](#)]
71. He, Z.; Kim, C.; Lin, L.H.; Jeon, T.H.; Lin, S.; Wang, X.C.; Choi, W. Formation of heterostructures via direct growth CN on h-BN porous nanosheets for metal-free photocatalysis. *Nano Energy* **2017**, *42*, 58–68. [[CrossRef](#)]
72. Yu, H.; Xu, S.; Zhang, S.; Wang, S.; He, Z. In-situ construction of core-shell structured TiB₂-TiO₂@g-C₃N₄ for efficient photocatalytic degradation. *Appl. Surf. Sci.* **2022**, *579*, 152201. [[CrossRef](#)]
73. He, Z.; Que, W.; Chen, J.; Yin, X.; He, Y.; Ren, J. Photocatalytic degradation of methyl orange over nitrogen-fluorine codoped TiO₂ nanobelts prepared by solvothermal synthesis. *ACS Appl. Mater. Interfaces* **2012**, *4*, 6816–6826. [[CrossRef](#)] [[PubMed](#)]
74. Wang, L.; Karuturi, S.; Zan, L. Bi₂S₃-In₂S₃ heterostructures for efficient photoreduction of highly toxic Cr⁶⁺ enabled by facet-coupling and Z-scheme structure. *Small* **2021**, *17*, 2101833. [[CrossRef](#)] [[PubMed](#)]

Disclaimer/Publisher's Note: The statements, opinions and data contained in all publications are solely those of the individual author(s) and contributor(s) and not of MDPI and/or the editor(s). MDPI and/or the editor(s) disclaim responsibility for any injury to people or property resulting from any ideas, methods, instructions or products referred to in the content.